Magneto-optical transport properties of monolayer phosphorene

M. Tahir,[1,*] P. Vasilopoulos,[1,†] and F. M. Peeters[2,‡]

[1]*Department of Physics, Concordia University, Montreal, Quebec H3G 1M8, Canada*
[2]*Departement Fysica, Universiteit Antwerpen Groenenborgerlaan 171, B-2020 Antwerpen, Belgium*

The electronic properties of monolayer phosphorene are exotic due to its puckered structure and large intrinsic direct band gap. We derive and discuss its band structure in the presence of a perpendicular magnetic field. Further, we evaluate the magneto-optical Hall and longitudinal optical conductivities as functions of temperature, magnetic field, and Fermi energy, and show that they are strongly influenced by the magnetic field. The imaginary part of the former and the real part of the latter exhibit regular interband oscillations as functions of the frequency ω in the range $\hbar\omega \sim$ 1.5–2 eV. Strong intraband responses in the latter and weak ones in the former occur at much lower frequencies. The magneto-optical response can be tuned in the microwave-to-terahertz and visible frequency ranges in contrast with a conventional two-dimensional electron gas or graphene in which the response is limited to the terahertz regime. This ability to isolate carriers in an anisotropic structure may make phosphorene a promising candidate for new optical devices.

PACS number(s): 78.20.Ls, 42.70.−a, 73.43.−f, 81.05.Zx

I. INTRODUCTION

Graphene possesses extraordinary properties but its application in device fabrication is limited by the zero band gap. Graphene-based transistors suffer from a low on-off current ratio due to its gapless structure [1,2]. This has lead to an intensive search for materials with a finite band gap including silicene [3], germanene [4], MoS$_2$, and other group-VI transition-metal dichalcogenides [5]. Despite the fact that these materials show a high on-off ratio, their carrier mobility is considerably lower than that of graphene and restricts their applications in electronics and optoelectronics [6]. Moreover, a very large intrinsic direct band gap in these materials renders them unsuitable for near-infrared optical telecommunication and midinfrared applications. Thus the search continues for a two-dimensional (2D) semiconducting material, with a direct band gap, high carrier mobility, and with the potential to form excellent contacts with known electrode materials.

Recent developments in the experimental realization of 2D phosphorene has attracted much interest due to its potential applications [7–9]. Unlike graphene, MoS$_2$ and other related materials, electrons in phosphorene are highly dispersive and delocalized along the out-of-plane direction [10]. Phosphorene has a honeycomb structure of black phosphorous with large intrinsic direct band gap of 1.52 eV assessed by tight-binding [11] and density functional theory [12–14]. Compared to graphene, the puckered structure of phosphorene exhibits lower symmetry that gives rise to in-plane anisotropic properties in momentum space. Carrier mobilities are very high at room temperature and exhibit a strongly anisotropic behavior in phosphorene-based transistors with a high on-off ratio [7,8,15]. Due to its highly dispersive band structure, phosphorene exhibits a high carrier mobility and a large optical conductivity [13]. A linear dichroism

has been shown in the computed absorption spectra, in that the positions of the lowest energy absorption peaks differ strongly for the two in-plane directions [13]. In addition to the traditional midinfrared and near-infrared emission, the unique anisotropic electronic and photonic properties of phosphorene may allow for the realization of novel optical components such as polarization sensors and anisotropic plasmonic devices [15]. Already due to its high optical efficiency [16], phosphorene has shown a high potential for optical device applications [17].

Optical transport properties of graphene show good agreement between theory and experiments [18]. Magneto-optical properties of topological insulators [19] and other single-layer materials, such as MoS$_2$ [20] and silicene [21], have also been studied. Landau levels (LLs) are formed in the presence of an external magnetic field. Transitions between the LLs generate absorption lines in the magneto-optical conductivity [21] and were used to distinguish between the topological insulator and normal (band) insulator phases in silicene in the presence of spin-orbit interaction and staggered potential [22]. From a fundamental point of view, many efforts have been made to explore different properties of phosphorene at zero magnetic field whereas limited work has appeared for finite magnetic field [23]. Accordingly, studies of magneto-optical properties are timely and expected to increase our understanding of this material. As will be shown, an important difference with graphene and other 2D systems is that their magneto-optical response occurs in the terahertz (THz) regime whereas phosphorene's can be tuned in the microwave-to-THz and visible frequency ranges.

In this work we study the magneto-optical transport properties of monolayer phosphorene. In Sec. II we derive and discuss its band structure in the presence of a perpendicular magnetic field. Further, using Kubo-type formulas in Sec. III we evaluate the optical Hall and longitudinal conductivities. We proceed with a discussion of the results and of the power absorption spectrum in Sec. IV. We then show briefly the oscillator strength of the optical transitions in Sec. V and conclude in Sec. VI.

---
*m.tahir06@alumni.imperial.ac.uk
†p.vasilopoulos@concordia.ca
‡francois.peeters@uantwerpen.be

II. BASIC EXPRESSIONS

We start with the widely used two-band model for 2D phosphorene [11,23], in which the low-energy Hamiltonian is

$$H = \begin{pmatrix} E^e + (\alpha'\Pi_x^2 + \beta\Pi_y^2)/2 & 0 \\ 0 & E^h - (\lambda'\Pi_x^2 + \eta\Pi_y^2)/2 \end{pmatrix},$$

(1)

where $\alpha' = \alpha + \gamma^2/E_g$, $\lambda' = \lambda + \gamma^2/E_g$, $\gamma = 8.5 *$ 10^5 m/s, $\alpha = 1/m_{ex} = 1/1.47m_e$, $\beta = 1/m_{ey} = 1/0.83m_e$, $\lambda = 1/m_{hx} = 1/10.66m_e$, $\eta = 1/m_{hx} = 1/1.12m_e$, and $E_g = E^e - E^h = 1.52$ eV. The minimum of the conduction band occurs at $E^e = 0.34$ eV and the maximum of the valence band at $E^h = -1.18$ eV. Further, $\Pi = \mathbf{p} + e\mathbf{A}$ is the 2D canonical momentum with vector potential $\mathbf{A}$. Using the Landau gauge $\mathbf{A} = (0, Bx, 0)$ and diagonalizing the Hamiltonian (1), we obtain the eigenvalues

$$E_n^s = E^s + s(n + 1/2)\hbar\omega_c^s, \quad n = 0, 1, 2, 3, \ldots, \quad (2)$$

where $s = +1(-1)$ for electrons (holes), $E^s = E^{e/h}$, $\omega_c^s = \omega_c^{e/h}$ with $\omega_c^e = eB/\sqrt{m'_{ex}m'_{ey}} = 2.696\omega_c$, $\omega_c^h = eB/\sqrt{m'_{hx}m'_{hy}} = 2.2076\omega_c$, $m'_{ex} = 1/\alpha'$, $m'_{hx} = 1/\lambda'$, and $\omega_c = eB/m_e$. It is interesting to note that unlike the anisotropic zero magnetic field dispersion, the LL spectrum is independent of the in-plane wave vectors. The corresponding normalized eigenfunctions are

$$\Psi_{n,k_y}(\mathbf{r}) = \frac{e^{ik_y \cdot y}}{\sqrt{L_y}} \begin{pmatrix} \phi_n(u^e) \\ \phi_n(u^h) \end{pmatrix}, \quad (3)$$

where $u^s = \xi^s(x - x_0)/l$ and $\xi^s = \sqrt{m'_{sx}\omega_c^s/\hbar}$; $l = \sqrt{\hbar/eB}$ is the magnetic length and $\phi_n(u)$ are the harmonic oscillator functions. If we use the Landau gauge $A = (-By, 0, 0)$, the eigenvalues are again given by Eq. (2) and the eigenfunctions are obtained from Eq. (3) by replacing x with y wherever they appear.

The density of states (DOS) is given by

$$D(E) = \frac{1}{S_0} \sum_{n,s,k_y} \delta(E - E_n^s), \quad (4)$$

where S_0 is the area of the system. The sum over k_y in Eq. (4) is evaluated using the prescription $(k_0 = L_x/2l^2)$ $\sum_{k_y} \to (L_y/2\pi)g_s \int_{-k_0}^{k_0} dk_y = (S_0/D_0)g_s$, where $D_0 = 2\pi l^2$ and $g_s = 2$ is the spin degeneracy. The Fermi energy E_F is determined from the electron concentration n_c,

$$n_c = \int_{-\infty}^{\infty} D(E)f(E)dE = g_s/D_0 \sum_{n,s} f(E_n^s), \quad (5)$$

where the Fermi-Dirac distribution function is written as $f(E_n^s) = (1 + \exp[\beta(E_n^s - E)])^{-1}$ with $\beta = 1/k_B T$. In Fig. 1 (top panel) the magenta solid curve shows E_F obtained numerically from Eq. (5) as a function of B for a realistic value of the electron density [23], $n_c = 1 \times 10^{16}$ m^{-2}, together with the LLs obtained from Eq. (2).

Assuming a Gaussian broadening of the LLs, Eq. (4) is rewritten as $D(E) = (g_s/D_c) \sum_{n,s} \exp[-(E - E_n^s)^2/2\Gamma^2]$, where $D_c = D_0\Gamma\sqrt{2\pi}$ and $\Gamma \propto \sqrt{B}$ is the width of the
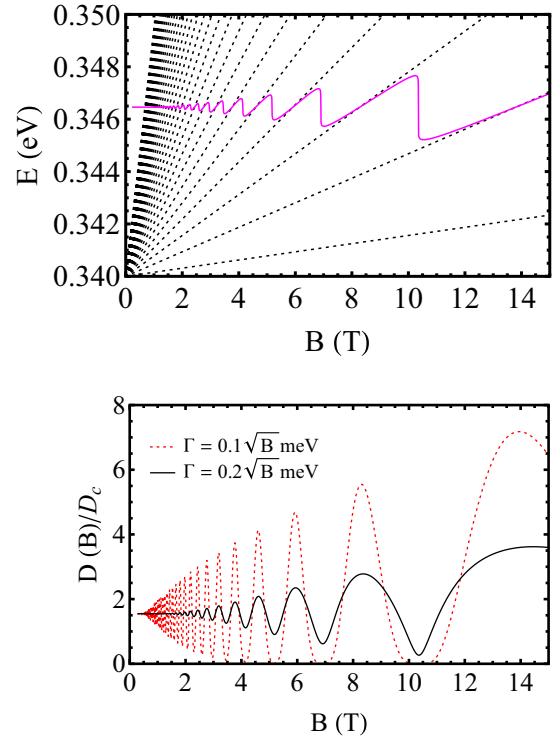

FIG. 1. (Color online) Top: Fermi energy (solid magenta) as a function of the magnetic field for $T = 1$ K and density $n_c = 1 \times 10^{16}$ m^{-2}. The dashed curves are the LLs evaluated from Eq. (2). Bottom: Dimensionless density of states as a function of the magnetic field B for two different values of the LL width.

Gaussian distribution [24]. The dimensionless DOS at $E = E_F$, $D(E_F) \equiv D(B)$, is shown in Fig. 1 (bottom panel) as a function of the magnetic field, for $\Gamma = 0.2\sqrt{B}$ meV (black solid curve) and $\Gamma = 0.1\sqrt{B}$ meV (red dotted curve). For weak fields B the level broadening is important whereas for large fields it may become smaller due to the $\sqrt{B}$ dependence since the distance between the LLs increases linearly with B.

III. LINEAR RESPONSE CONDUCTIVITIES

We consider a many-body system described by the Hamiltonian $H = H_0 + H_I - \mathbf{R} \cdot \mathbf{F}(t)$, where H_0 is the unperturbed part, H_I is a binary-type interaction (e.g., between electrons and impurities or phonons), and $-\mathbf{R} \cdot \mathbf{F}(t)$ is the interaction of the system with the external field $F(t)$ [25]. For conductivity problems we have $\mathbf{F}(t) = e\mathbf{E}(t)$, where $\mathbf{E}(t)$ is the electric field, e the electron charge, $\mathbf{R} = \sum_i \mathbf{r}_i$, and $\mathbf{r}_i$ is the position operator of electron i. In the representation in which H_0 is diagonal the many-body density operator $\rho = \rho^d + \rho^{nd}$ has a diagonal part ρ^d and a nondiagonal part ρ^{nd}. For weak electric fields and weak scattering potentials, for which the first Born approximation applies, the conductivity tensor has a diagonal part $\sigma_{\mu\nu}^d$ and a nondiagonal part $\sigma_{\mu\nu}^{nd}$ part, $\sigma_{\mu\nu} = \sigma_{\mu\nu}^d + \sigma_{\mu\nu}^{nd}$, $\mu, \nu = x, y$.

In general we have two kinds of currents, diffusive and hopping, but usually only one of them is present. In the present problem, due to the magnetic field we have only the hopping current since the diffusive one vanishes due to $v_{\mu\zeta} = 0$, see

Eq. (6). For elastic scattering the diffusive part of $\sigma_{\mu\nu}^d$ is given by

$$\sigma_{\mu\nu}^{dif}(\omega) = \frac{\beta e^2}{S_0} \sum_\zeta f_\zeta (1 - f_\zeta) \frac{v_{\nu\zeta}\, v_{\mu\zeta}\, \tau_\zeta}{1 + i\omega\tau_\zeta}, \qquad (6)$$

where $S_0 = L_x L_y$, τ_ζ is the relaxation time, ω the frequency, and $v_{\mu\zeta}$ the diagonal matrix elements of the velocity operator. Further, $f_\zeta = [1 + \exp\beta(E_\zeta - E_F)]^{-1}$ is the Fermi-Dirac distribution function with $\beta = 1/k_B T$, T the temperature and E_F the Fermi level.

The collisional part $\sigma_{\mu\nu}^{\text{col}}(\omega)$ of $\sigma_{\mu\nu}^d$ is much smaller than the nondiagonal part $\sigma_{\mu\nu}^{nd}(\omega)$ and we neglect it. As for $\sigma_{\mu\nu}^{nd}(\omega)$ given in Ref. [25], one can use the identity $f_\zeta(1 - f_{\zeta'})[1 - \exp\beta(E_\zeta - E_{\zeta'})] = f_\zeta - f_{\zeta'}$ and cast [26] its original form in the more familiar one

$$\sigma_{\mu\nu}^{nd}(\omega) = \frac{i\hbar e^2}{S_0} \sum_{\zeta \neq \zeta'} \frac{(f_\zeta - f_{\zeta'})\, v_{\nu\zeta\zeta'}\, v_{\mu\zeta'\zeta}}{(E_\zeta - E_{\zeta'})(E_\zeta - E_{\zeta'} + \hbar\omega + i\Gamma)}, \qquad (7)$$

where the sum runs over all quantum numbers $|\zeta\rangle \equiv |n,s,k_y\rangle$ and $|\zeta'\rangle \equiv |n',s',k_y'\rangle$ provided $\zeta \neq \zeta'$. The infinitesimal quantity ϵ in the original form has been replaced by Γ to account for the broadening of the energy levels. Equation (7) has been recently applied to phosphorene in the absence of a magnetic field in Ref. [16]. The evaluation of $v_{\nu\zeta\zeta'}$ and $v_{\mu\zeta\zeta'}$ is outlined in the Appendix. Using Eqs. (1) and (3) we obtain

$$v_{x,n,n'}^{s,s} = i v_x^s (\sqrt{n}\delta_{n-1,n'} - \sqrt{n+1}\delta_{n+1,n'})\delta_{k_y,k_y'}, \qquad (8)$$

$$v_{y,n',n}^{s,s} = v_y^s (\sqrt{n+1}\delta_{n',n+1} + \sqrt{n}\delta_{n',n-1})\delta_{k_y,k_y'}, \qquad (9)$$

where $v_x^s = \omega_c^s/\sqrt{2}\xi^s$ and $v_y^s = (m_{sx}'\omega_c^s/\sqrt{2}\xi^s)(\beta/\eta)$. The results for $s \neq s'$ are given in the Appendix. Since $|\zeta\rangle \equiv |n,s,k_y\rangle$, there will be one summation over k_y which, with periodic boundary conditions for k_y, gives the factor $S_0/2\pi l^2$. Substituting Eq. (8) into Eq. (7), summing over n', and setting $\sigma_0 = -g_s\hbar e^2/2\pi l^2$, we obtain the longitudinal nondiagonal conductivity as

$$\sigma_{xx}^{nd}(\omega) = i\sigma_0 \sum_{s,s',n=1} \frac{n[f_n^s - f_{n-1}^{s'}](A_{xx}^{s,s'})^2}{I_{n,n-1}^{s,s'}(I_{n,n-1}^{s,s'} + \hbar\omega + i\Gamma)}$$
$$+ i\sigma_0 \sum_{s,s',n=0} \frac{(n+1)[f_n^s - f_{n+1}^{s'}](A_{xx}^{s,s'})^2}{I_{n,n+1}^{s,s'}(I_{n,n+1}^{s,s'} + \hbar\omega + i\Gamma)}, \qquad (10)$$

where $A_{xx}^{s,s} = v_x^s$, $A_{xx}^{s,s'} = v_x^e - v_x^h$, and $I_{n,n\pm1}^{s,s'} = E_n^s - E_{n\pm1}^{s'}$. After making the changes $n - 1 \to m \to n$ in the first sum, we combine the two sums and obtain

$$\sigma_{xx}^{nd}(\omega) = i\sigma_0 \sum_{s,s',n=0} (n+1)\left[\frac{[f_{n+1}^s - f_n^{s'}](A_{xx}^{s,s'})^2}{I_{n+1,n}^{s,s'}(I_{n+1,n}^{s,s'} + \hbar\omega + i\Gamma)} \right.$$
$$\left. + \frac{[f_n^s - f_{n+1}^{s'}](A_{xx}^{s,s'})^2}{I_{n,n+1}^{s,s'}(I_{n,n+1}^{s,s'} + \hbar\omega + i\Gamma)} \right]. \qquad (11)$$

In the limit $\Gamma \to 0$, $\omega \to 0$ and $s = s'$ Eq. (11) yields zero. The matrix elements of the velocity operators are nonzero only

for $n' = n \pm 1$. Regarding the sums over s,s' for convenience we write $\sum_{s,s'} = \sum_{+,+} + \sum_{-,-} + \sum_{+,-} + \sum_{-,+}$. Here the subscript $+/-$ denotes the conduction/valence band. After performing the summation over s and s' we obtain the absorption spectrum of the real part of $\sigma_{xx}^{nd}(\omega)$ in the form

$$\Re\sigma_{xx}^{nd}(\omega) = \pi\sigma_0 \sum_{n=0}^\infty (n+1)\left[-\frac{[f_n^+ - f_{n+1}^+]\delta(\hbar\omega_c^e - \hbar\omega)}{\hbar\omega_c^e/(A_{xx}^{+,+})^2} \right.$$
$$+ \frac{[f_n^- - f_{n+1}^-]\delta(\hbar\omega_c^h + \hbar\omega)}{\hbar\omega_c^h/(A_{xx}^{-,-})^2}$$
$$- \frac{[f_{n+1}^- - f_n^+]\delta(I_{n,n+1}^{+,-} - \hbar\omega)}{I_{n,n+1}^{+,-}/(A_{xx}^{+,-})^2}$$
$$\left. + \frac{[f_n^- - f_{n+1}^+]\delta(I_{n,n+1}^{-,+} + \hbar\omega)}{I_{n,n+1}^{-,+}/(A_{xx}^{-,+})^2} \right]. \qquad (12)$$

Here $I_{n,n+1}^{s,s} = E_n^s - E_{n+1}^s$ and $\pi\delta(x) = \Gamma/(x^2 + \Gamma^2)$. Using Eqs. (8) and (9) into Eq. (7), and carrying out the sum over n' similar to Eq. (10) and then making the changes $n - 1 \to m \to n$ in the first sum, we obtain the optical Hall conductivity as

$$\sigma_{xy}^{nd}(\omega) = \sigma_0 \sum_{s,s',n=0} (n+1)\left[\frac{[f_{n+1}^s - f_n^{s'}]A_{xy}^{s,s'}}{I_{n+1,n}^{s,s'}(I_{n+1,n}^{s,s'} + \hbar\omega + i\Gamma)} \right.$$
$$\left. - \frac{[f_n^s - f_{n+1}^{s'}]A_{xy}^{s,s'}}{I_{n,n+1}^{s,s'}(I_{n,n+1}^{s,s'} + \hbar\omega + i\Gamma)} \right], \qquad (13)$$

where $A_{xy}^{s,s} = (v_x^s)^2 m_{sx}'\beta$ and $A_{xy}^{s,s'} = (v_x^e - v_x^h) * (\beta m_{ex}'v_x^e - \eta m_{hx}'v_x^h)$. In the $\omega = \Gamma = 0$ and $s = s' = e$ limit Eq. (13) yields the quantized Hall conductivity of a 2DEG [26]

$$\sigma_{xy}^{nd}(0) = g_s \frac{e^2}{2h} \sum_{n=0}^\infty (n+1)[f_n - f_{n+1}]. \qquad (14)$$

Also, apart from the absence of valley degeneracy and the appearance of $(n+1)$ instead of $(n + 1/2)$, the dc limit of Eq. (13) gives results similar to those of graphene [27].

Following the procedure adopted for the component σ_{xx}^{nd} and using Eq. (10) we obtain

$$\text{Im}\,\sigma_{xy}^{nd}(\omega) = \pi\sigma_0 \sum_n (n+1)\left[-\frac{[f_n^+ - f_{n+1}^+]\,\delta(\hbar\omega_c^e - \hbar\omega)}{\hbar\omega_c^e/A_{xy}^{+,+}} \right.$$
$$- \frac{[f_n^- - f_{n+1}^-]\,\delta(\hbar\omega_c^h - \hbar\omega)}{\hbar\omega_c^h/A_{xy}^{-,-}}$$
$$+ \frac{[f_{n+1}^- - f_n^+]\,\delta(I_{n,n+1}^{+,-} - \hbar\omega)}{I_{n,n+1}^{+,-}/A_{xy}^{+,-}}$$
$$\left. + \frac{[f_n^- - f_{n+1}^+]\,\delta(I_{n,n+1}^{-,+} + \hbar\omega)}{I_{n,n+1}^{-,+}/A_{xy}^{-,+}} \right]. \qquad (15)$$

IV. DISCUSSION OF RESULTS

The energies of the positive branch levels in Eq. (2) are different from those of the negative branch due to the difference in the E^s values and cyclotron frequency in each band (electron/hole). Due to $\hbar\omega_c^s \ll E^s$, the intraband and
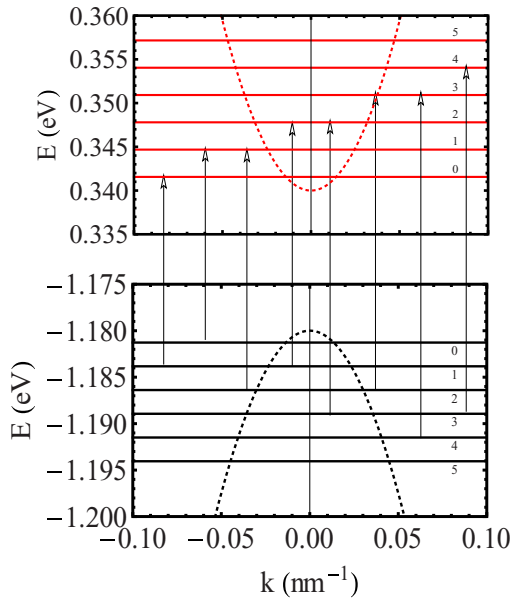
FIG. 2. (Color online) Band structure at a fixed magnetic field $B = 10$ Tesla for conduction (red) and valence band (black). The dashed curves show the $B = 0$ spectrum of Eq. (1): it is symmetric around the Γ point and consistent with Fig. 1 of Ref. [23] (a). The arrows indicate possible interband transitions.

interband optical transitions belong to two widely separated regimes: the former is in the microwave-to-THz range and the latter in the visible frequency range. We will first consider the latter, which involve transitions between neighboring LLs ($n' = n \pm 1$) and $s \neq s'$. In all results shown below the common parameter are temperature $T = 10$ K and level broadening $\Gamma = 0.2\sqrt{B}$ meV.

Unlike graphene [18], silicene [21,22], and topological insulators [19], the large intrinsic band gap and the lack of perfect symmetry between the positive and negative branches of the phosphorene spectrum, shown in Fig. 2 for $B = 0$ (dashed curve) and $B \neq 0$ (straight solid lines), have important implications for the peaks seen in the real part of $\sigma_{xx}^{nd}(\omega)$ and the imaginary parts of $\sigma_{xy}^{nd}(\omega)$. In Fig. 3 we plot the former as a function of the frequency. We consider a rather strong field $B = 10$ T so that well-resolved LLs are formed. The value $E_F = 0.343$ eV is between the $n = 0$ and $n = 1$ LLs, whereas the value $E_F = 0.356$ eV is between the $n = 4$ and $n = 5$ LLs.
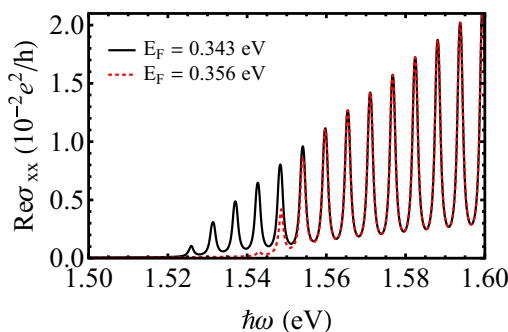

FIG. 3. (Color online) Real part of the longitudinal optical conductivity as a function of the photon energy for a field $B = 10$ Tesla.
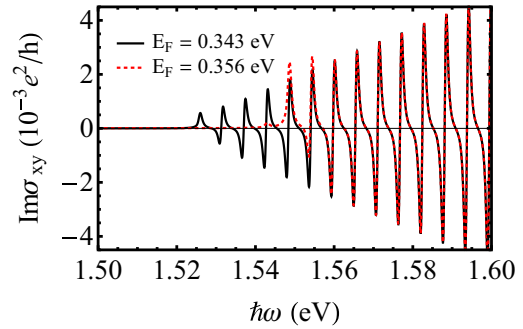

FIG. 4. (Color online) Imaginary part of the optical Hall conductivity versus photon energy for a field $B = 10$ Tesla.

In the latter case the peaks for $n \leqslant 3$ are Pauli blocked and no longer possible. We notice the equally spaced absorption peaks. The optical selection rules allow n to change only by 1. In addition one needs to go from occupied to unoccupied states through the absorption of a photon. The first peak occurring at $\hbar\omega = 1.526$ eV represents transitions involving the $n = 0$ LL. In fact, it is the sum of the absorption peaks of two transitions involving the energy differences $E_1^+ - E_0^-$ and $E_0^+ - E_1^-$ and is described by the last two terms in Eq. (12). This can also be understood from the spectrum shown in Fig. 2. A similar explanation holds for the peaks at $\hbar\omega = 1.532$ eV, $\hbar\omega = 1.537$ eV, etc. The peak spacing is proportional to B and experimentally one should observe such well-spaced peaks even for modest fields B. In contrast to phosphorene, in graphene and other 2D systems the spectral weight of the interband peaks is redistributed into intraband peaks [22,28]. This shows how the conductivity changes as E_F moves through the LLs.

Inspection of Eqs. (12) and (15) shows that the Hall and longitudinal conductivities are different due to the factors $A_{xy}^{ss'}$ and $A_{xx}^{ss'}$, which reflect the difference between Eqs. (8) and (9).

In Fig. 4 one first sees a positive peak and then a decrease (dip). This represents interband transitions involving the $n = 0$ LL similar to Fig. 3 and the energy differences $E_1^+ - E_0^-$ and $E_0^+ - E_1^-$. It can be understood as the sum of the last two terms in Eq. (15). For the pure Dirac case these two peaks would occur at the same energy and hence would cancel out perfectly due to the symmetry of the spectrum. Only the first peak would remain in the Hall conductivity and all higher peaks would cancel out [22,28].

In Fig. 5 we show the real part of the longitudinal conductivity (top panel) and the imaginary one of the Hall conductivity (bottom panel) versus the field B for $\hbar\omega = 1.6$ eV. Due to the interband transitions from occupied to unoccupied states through the absorption of the photon, the oscillation patterns are similar to those shown in Figs. 3 and 4.

The peak structure just described above for $\Re\sigma_{xx}^{nd}(\omega)$ and Im $\sigma_{xy}^{nd}(\omega)$ importantly affects their behavior for right-polarized $(+)$ and left-polarized $(-)$ light. For real experiments that probe the (circular) polarization of resonant light, as in the case of the Kerr and Faraday effects, one evaluates the quantity $\sigma_\pm(\omega)$ given by

$$\sigma_\pm(\omega) = \Re\sigma_{xx}^{nd}(\omega) \mp \text{Im}\,\sigma_{xy}^{nd}(\omega), \qquad (16)$$
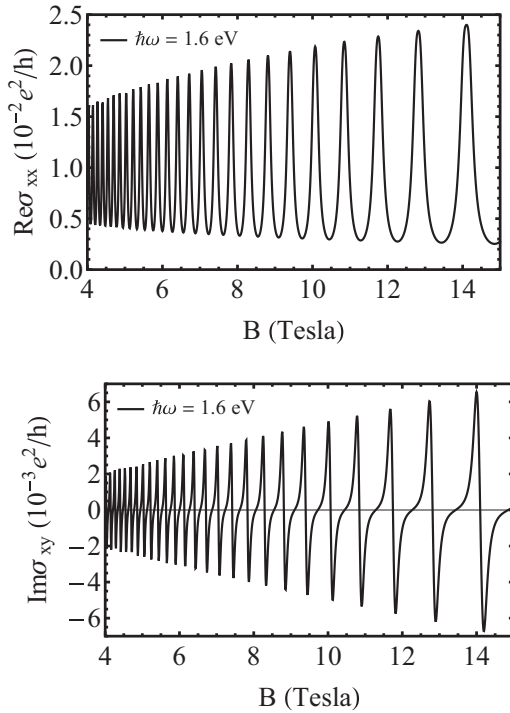
FIG. 5. Real part of the longitudinal optical conductivity (top) and imaginary part of the optical Hall conductivity (bottom) versus field B for photon energy $\hbar\omega = 1.6$ eV.

with the upper (lower) signs corresponding to right (left) polarization [18,19]. In Fig. 6 we show $\sigma_-(\omega)$ (solid black curve) and $\sigma_+(\omega)$ (dotted red curve) as functions of the frequency using the parameters of Figs. 3 and 4. As seen, there is a direct correspondence between these results and those of Figs. 3 and 4. The peaks in $\sigma_+(\omega)$ are shifted a bit (downward) in energy relative to those in $\sigma_-(\omega)$. This difference also shows up in the power absorption spectrum given by

$$P(\omega) = (E/2)[\sigma_{xx}(\omega) + \sigma_{yy}(\omega) - i\sigma_{yx}(\omega) + i\sigma_{xy}(\omega)].$$
(17)

We recall that $\sigma_{\mu\nu} = \sigma_{\mu\nu}^d + \sigma_{\mu\nu}^{nd} = \sigma_{\mu\nu}^{nd}$ since the component $\sigma_{\mu\mu}^d, \mu = x, y$, vanishes. The component $\sigma_{yy}^{nd}(\omega)$ is given by $\sigma_{xx}^{nd}(\omega)$ with $A_{xx}^{s,s'}$ replaced by $A_{yy}^{s,s'}$, and $\mathrm{Im}\,\sigma_{xy}^{nd}(\omega) =$
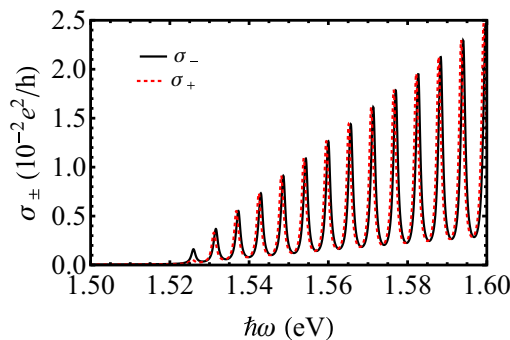

FIG. 6. (Color online) Real part of the right-polarized optical conductivity $\sigma_+(\omega)$ and of the left-polarized one $\sigma_-(\omega)$ versus photon energy for $E_F = 0.343$ eV and field $B = 10$ Tesla.
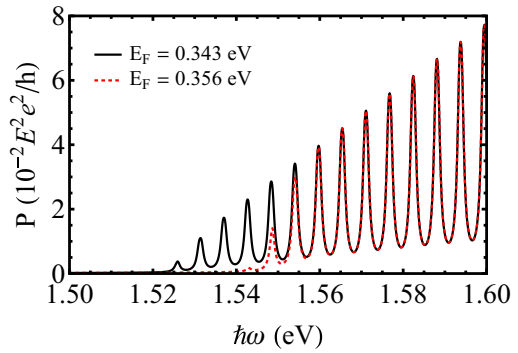

FIG. 7. (Color online) Power spectrum versus photon energy for an electric field $E = 8$ V/nm, for two values of E_F and field $B = 10$ Tesla.

$-\mathrm{Im}\,\sigma_{yx}^{nd}(\omega)$. The spectrum $P(\omega)$ is shown in Fig. 7 as a function of the photon energy for two values of E_F. Given that $\mathrm{Im}\,\sigma_{xy}^{nd}(\omega)$ is much smaller than $\Re\sigma_{xx}^{nd}(\omega)$, cf. Figs. 3 and 4, the peaks in it are essentially the same as those in the longitudinal conductivity. The absence of the $n \leqslant 3$ peaks for $E_F = 0.356$ is due to Pauli blocking and consistent with Figs. 3 and 4.

Now we consider intraband transitions between the nth and $(n + 1)$th LLs, for $E_F > 0$, which involve an energy range much smaller than E_F. This involves large values of n and is known as the semiclassical limit of the magneto-optical conductivity in which E_F is much larger than $\hbar\omega_c$. Let us assume that $E_F \approx E_n^+$ lies between the nth and $(n + 1)$th LLs. The pertinent energy difference is $E_n^+ - E_{n+1}^+ = -\hbar\omega_c^e$. For such transitions we obtain

$$\Re\sigma_{xx}^{nd}(\omega) = \pi\sigma_0 \sum_n (n + 1) \frac{[f_{n+1}^+ - f_n^+]}{\hbar\omega_c^e/(A_{xx}^{+,+})^2} \delta(\hbar\omega_c^e - \hbar\omega).$$
(18)

The real part of $\sigma_{xx}^{nd}(\omega)$ is shown in Fig. 8 by the top two curves. As seen, the optical spectral weight under these curves increases with E_F. These peaks lie in the range of microwave-to-THz frequencies and their amplitude is larger than that of the interband transitions shown in Fig. 3. This is
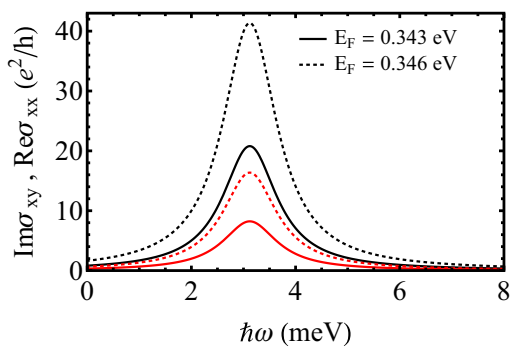

FIG. 8. (Color online) Intraband limit of the real part (top two curves) of the longitudinal optical conductivity and of the imaginary part (bottom two curves) of the Hall conductivity versus photon energy for two values of E_F and $B = 10$ Tesla. The energy $\hbar\omega$ is measured from the bottom of the conduction band.

consistent with graphene or topological insulators and other symmetric 2D systems in which the relevant spectral weight increases with E_F, see, e.g., Fig. 7 of Ref. [28], and the optical features appear in the THz regime only [22,28,29]. The two lowest curves show the imaginary part of the Hall conductivity $\sigma_{xy}^{nd}(\omega)$ for the same values of E_F. As seen, apart from the scale, $\sigma_{xy}^{nd}(\omega)$ shows the same behavior as $\sigma_{xx}^{nd}(\omega)$. The magnitudes of $\sigma_{xy}^{nd}(\omega)$ and $\sigma_{xx}^{nd}(\omega)$ are different due to the different values of the velocity components along the x and y axes. The peaks of all curves occur at $\omega = \omega_c$.

V. OSCILLATOR STRENGTH

The oscillator strength depends strongly on the symmetries of the initial- and final-state wave functions and is a function of the in-plane momentum vector [30]. The strength of an optical transition is typically characterized by the dipole matrix element between the initial and final states. Since a dimensionless quantity is more useful for making comparisons in different systems, the oscillator strength is often used instead of the dipole matrix element. It is defined through the $\mathbf{A} \cdot \mathbf{p}$ term in the Hamiltonian describing the interaction between the electron and the electromagnetic field as

$$O_{n',n} = \frac{2m}{\hbar^2} \sum_{s,s'} \left(E_{n'}^{s'} - E_n^s \right) |\langle n', s', k_y' | \mathbf{r} | n, s, k_y \rangle|^2, \quad (19)$$

where $m = \sqrt{m_{sx}' m_{sy}}$ is the mass of the particles and $(E_{n'}^{s'} - E_n^s)/\hbar$ the frequency involved in the transitions from the initial to the final states. With the help of Eq. (3), the relevant matrix element of the position operator ($\langle n' | \mathbf{r} | n \rangle \equiv \langle n', s, k_y' | x | n, s, k_y \rangle$) is

$$\langle n', s, k_y' | x | n, s, k_y \rangle = [x_0 \delta_{n',n} + (1/\sqrt{2}\xi^s)(\sqrt{n+1}\delta_{n',n+1}$$
$$+ \sqrt{n}\delta_{n',n-1})]\delta_{k_y',k_y}. \quad (20)$$

Equations (19) and (20) clearly show the intraband and interband transitions shown in Figs. 2–8. The transitions follow the selection rule $n' = n \pm 1$. It is interesting to physically interpret the oscillator strength in terms of intraband and interband transitions. The intraband transitions between the n and $n+1$ states by the absorption of a photon shown in Fig. 8 are the same as those shown by Eqs. (19) and (20). For these transitions we have $E_{n+1}^+ - E_n^+ = \hbar\omega_c^e, s = s' = +$, whereas the interband transitions of Figs. 3–7 follow the rule $n' = n \pm 1$ but with $s \neq s'$. The first absorption peak in the optical longitudinal conductivity is the sum of the two transitions $E_n^- \to E_{n+1}^+$ and $E_{n+1}^- \to E_n^+$. This corresponds to the first two peaks in the optical Hall conductivity with the first being positive and the second negative. The corresponding energy absorption for the first peak is $E_1^+ - E_0^-$ and for the second one $E_0^+ - E_1^-$. Similarly other peaks follow the well-defined selection rules between higher LLs. The spacing between the peaks also depends on the broadening, which we have fixed. When the Fermi level is in the band and not zero, the peak heights are suppressed and shifted downward.

VI. SUMMARY

We studied magneto-optical transport properties of mono-layer phosphorene subject to an external perpendicular magnetic field. The relevant conductivities exhibit periodic oscillations that can be controlled by the magnetic field B. In each band the oscillation peaks are equidistant, reflecting the equally spaced LLs, and show a linear dependence on B. The intraband and interband optical transitions pertain to two completely different regimes: the former occur in the microwave-to-terahertz range and the latter ones in the visible frequency range. This is in contrast with a conventional 2D electron gas, topological insulators, and graphene in which these features appear only in the THz regime. It is also in contrast with phosphorene's responses at $B = 0$, which occur in the midinfrared to near-infrared regime [8,16,17]. These findings expand the horizon of the optical properties of 2D phosphorene and are expected to be useful in the design of new optical devices.

APPENDIX A

The velocity operator, obtained from Eq. (1), reads

$$v = \frac{\partial H}{\partial \mathbf{p}} = \begin{pmatrix} \alpha' p_x + \beta p_y & 0 \\ 0 & -\lambda' p_x - \eta p_y \end{pmatrix}. \quad (A1)$$

For $s = s'$ the explicit evaluation of the velocity matrix elements gives Eqs. (8) and (9) with $s = + \equiv e$ and $s = - \equiv h$. For $s \neq s'$ we obtain explicitly

$$v_{x,n,n'}^{-,+} = i \left(v_x^e - v_x^h \right) \delta_{k_y,k_y'} \int_{-\infty}^{\infty} dx \, \phi_n(u^h)$$
$$\times [\sqrt{n'+1}\phi_{n'+1}(u^e) - \sqrt{n'}\phi_{n'-1}(u^e)]. \quad (A2)$$

Because $u^h = 1.1u^e$ we set $u^h = u^e$ in order to have simple expressions. We then have

$$I = \int dx \, \phi_m^*(u^h)\phi_n(u^e) \approx \delta_{n,m}. \quad (A3)$$

This gives $v_{x,n,n'}^{-,+} = v_{x,n,n'}^{+,-}$ and $v_{y,n',n}^{-,+} = v_{y,n',n}^{+,-}$ with

$$v_{x,n,n'}^{-,+} = i \left\{ v_x^e - v_x^h \right\} [\sqrt{n}\delta_{n,n'+1} - \sqrt{n'}\delta_{n,n'-1}]\delta_{k_y,k_y'}, \quad (A4)$$

$$v_{y,n',n}^{-,+} = \left\{ v_y^e - v_y^h \right\} [\sqrt{n'}\delta_{n',n+1} + \sqrt{n}\delta_{n',n-1}]\delta_{k_y,k_y'}. \quad (A5)$$

To check the approximation (A3) we evaluate explicitly the integral I for $n = m$ (I vanishes for $n \neq m$, see Ref. [31]) and $n = 0,1,2,5,10$ using the explicit expressions of the Hermite polynomials, e.g., $H_0(x) = 1, H_1(x) = 2x, H_2(x) = 4x^2 - 2$, etc. The values we obtain for $n = 0,1,2,5,10$ are, respectively, 0.997, 0.992, 0.983, 0.924, and 0.742. This shows that the approximation (A3) is a valid one at least when the magnetic field is strong and only a few LLs are occupied.

[1] A. H. Castro Neto, F. Guinea, N. M. R. Peres, K. S. Novoselov, and A. K. Geim, Rev. Mod. Phys. **81**, 109 (2009).

[2] F. Schwierz, Nature Nanotech. **5**, 487 (2010).

[3] J. Sone, T. Yamagami, Y. Aoki, K. Nakatsuji, and H. Hirayama, New J. Phys. **16**, 095004 (2014); P. D. Padova, C. Ottaviani, C. Quaresima, B. Olivieri, P. Imperatori, E. Salomon, T. Angot, L. Quagliano, C. Romano, A. Vona, M. Muniz-Miranda, A. Generosi, B. Paci, and G. L. Lay, 2D Materials **1**, 021003 (2014).

[4] M. E. Dávila, L. Xian, S. Cahangirov, A. Rubio, and G. Le. Lay, New J. Phys. **16**, 095002 (2014).

[5] Q. H. Wang, K. Kalantar-Zadeh, A. Kis, J. N. Coleman, and M. S. Strano, Nature Nanotech. **7**, 699 (2012); A. K. Geim and I. V. Grigorieva, Nature (London) **499**, 419 (2013).

[6] B. Radisavljevic, A. Radenovic, J. Brivio, V. Giacometti, and A. Kis, Nature Nanotech. **6**, 147 (2011); H. Fang, S. Chuang, T. C. Chang, K. Takei, T. Takahashi, and A. Javey, Nano Lett. **12**, 3788 (2012).

[7] L. Li, Y. Yu, G. J. Ye, Q. Ge, X. Ou, H. Wu, D. Feng, X. H. Chen, and Y. Zhang, Nature Nanotechnol. **9**, 372 (2014).

[8] F. Xia, H. Wang, and Y. Jia, Nature Commun. **5**, 4458 (2014); S. P. Koenig, R. A. Doganov, H. Schmidt, A. H. C. Neto, and B. Ozyilmaz, Appl. Phys. Lett. **104**, 103106 (2014).

[9] H. Liu, A. T. Neal, Z. Zhu, Z. Luo, X. Xu, D. Tomanek, and P. D. Ye, ACS Nano **8**, 4033 (2014); E. S. Reich, Nature (London) **506**, 19 (2014); Y. S. Liu, X. Zhang, X. F. Yang, X. K. Hong, J. F. Feng, M. S. Sib, and X. F. Wang, Phys. Chem. Chem. Phys. **17**, 10462 (2015).

[10] C. Q. Han, M. Y. Yao, X. X. Bai, L. Miao, F. Zhu, D. D. Guan, S. Wang, C. L. Gao, C. Liu, D. Qian, Y. Liu, and J.-F. Jia, Phys. Rev. B **90**, 085101 (2014).

[11] A. N. Rudenko and M. I. Katsnelson, Phys. Rev. B **89**, 201408 (2014); M. Ezawa, New J. Phys. **16**, 115004 (2014).

[12] Y. Du, C. Ouyang, S. Shi, and M. Lei, J. Appl. Phys. **107**, 093718 (2010).

[13] J. Qiao, X. Kong, Z.-X. Hu, F. Yang, and W. Ji, Nature Commun. **5**, 4475 (2014).

[14] A. S. Rodin, A. Carvalho, and A. H. Castro Neto, Phys. Rev. Lett. **112**, 176801 (2014).

[15] T. Low, R. Roldán, H. Wang, F. Xia, P. Avouris, L. M. Moreno, and F. Guinea, Phys. Rev. Lett. **113**, 106802 (2014).

[16] M. Buscema, D. J. Groenendijk, S. I. Blanter, G. A. Steele, H. S. J. van der Zant, and A. Castellanos-Gomez, Nano Lett. **14**, 3347 (2014); T. Low, A. S. Rodin, A. Carvalho, Y. Jiang, H. Wang, F. Xia, and A. H. Castro Neto, Phys. Rev. B **90**, 075434 (2014).

[17] N. Youngblood, C. Chen, S. J. Koester, and M. Li, Nature Photon. **9**, 247 (2015).

[18] V. P. Gusynin, S. G. Sharapov, and J. P. Carbotte, Phys. Rev. Lett. **98**, 157402 (2007); Z. Q. Li, E. A. Henriksen, Z. Jiang, Z. Hao, M. C. Martin, P. Kim, H. L. Stormer, and D. N. Basov, Nature Phys. **4**, 532 (2008).

[19] W.-K. Tse and A. H. MacDonald, Phys. Rev. B **84**, 205327 (2011); I. Garate and M. Franz, ibid. **84**, 045403 (2011); D. K. Efimkin and Y. E. Lozovik, ibid. **87**, 245416 (2013); M. Lasia and L. Brey, ibid. **90**, 075417 (2014).

[20] R.-L. Chu, X. Li, S. Wu, Q. Niu, W. Yao, X. Xu, and C. Zhang, Phys. Rev. B **90**, 045427 (2014).

[21] A. Pound, J. P. Carbotte, and E. J. Nicol, Phys. Rev. B **85**, 125422 (2012).

[22] C. J. Tabert and E. J. Nicol, Phys. Rev. Lett. **110**, 197402 (2013).

[23] X. Y. Zhou, R. Zhang, J. P. Sun, Y. L. Zou, D. Zhang, W. K. Lou, F. Cheng, G. H. Zhou, F. Zhai, and K. Chang, Sci. Rep. **5**, 12295 (2015); L. Li, F. Yang, G. J. Ye, Z. Zhang, K. Watanabe, T. Taniguchi, Y. Wang, X. H. Chen, and Y. Zhang, arXiv:1504.07155v1; J. M. Pereira, Jr., and M. I. Katsnelson, arXiv:1504.02452v1; Y. Jiang, R. Roldan, F. Guinea, and T. Low, arXiv:1505.00175v1; N. Gillgren, D. Wickramaratne, Y. Shi, T. Espiritu, J. Yang, J. Hu, J. Wei, X. Liu, Z. Mao, K. Watanabe, T. Taniguchi, M. Bockrath, Y. Barlas, R. K. Lake, and C. N. Lau, 2D Material **2**, 011001 (2015).

[24] Y. Zheng and T. Ando, Phys. Rev. B **65**, 245420 (2002).

[25] M. Charbonneau, K. M. Van Vliet, and P. Vasilopoulos, J. Math. Phys. **23**, 318 (1982).

[26] P. Vasilopoulos, Phys. Rev. B **32**, 771 (1985).

[27] P. M. Krstajić and P. Vasilopoulos, Phys. Rev. B **83**, 075427 (2011); **86**, 115432 (2012).

[28] P. E. C. Ashby and J. P. Carbotte, Phys. Rev. B **87**, 245131 (2013); Z. Li and J. P. Carbotte, ibid. **88**, 045414 (2013).

[29] T. Morimoto, Y. Hatsugai, and H. Aoki, Phys. Rev. Lett. **103**, 116803 (2009).

[30] F. M. Peeters, A. Matulis, M. Helm, T. Fromherz, and W. Hilber, Phys. Rev. B **48**, 12008 (1993).

[31] I. S. Gradshteyn and I. M. Ryzhik, *Tables of Integrals, Series and Products* (Academic Press, New York, 1980), p. 803.